CrystEngComm

ROYAL SOCIETY OF CHEMISTRY

PAPER

View Article Online
View Journal | View Issue

Check for updates

Cite this: *CrystEngComm*, 2022, **24**, 5900

Effects of alkyl chain length on the cold crystallization of Schiff-base nickel(II) complexes†

Toru Ishikawa, * Akinori Honda and Kazuo Miyamura*

Received 4th March 2022,
Accepted 18th July 2022

DOI: 10.1039/d2ce00305h

rsc.li/crystengcomm

"Cold crystallization" is the exothermic phenomenon occurring during the heating process of a supercooled liquid. Molecules that exhibit cold crystallization can be used as heat storage materials. Schiff-base nickel(II) complexes containing a quaternary carbon bearing two methyl groups and alkyl chains of variable length (OC*n*-salmpn, where *n* = 2, 4, 6, 8, 10, 12, 14, 16, and 18) displayed complex thermal behavior, including cold crystallization. The steric bulk of the two methyl groups decreases crystallization rate, resulting in a supercooled state. The alkyl chains control both the thermal behavior and the aggregation structure, and the complexes are expected to be used as new heat storage materials. In addition to displaying complex thermal behavior, some OC*n*-salmpn complexes can incorporate chloroform molecules depending on the alkyl chain length, enabling additional functionality.

Introduction

Alkyl chains tend to assemble in parallel as a result of the van der Waals interactions among them, the interaction influences the crystal structure. Therefore, the structures of alkyl derivatives vary depending on the chain length. Accordingly, the alkylation of rigid molecules can alter their physical properties[1–11] significantly, including their thermal properties,[12–15] crystal structure,[16–21] and the structure of adsorbed monolayers.[22–28] We have analyzed the thermal properties of salen derivatives bearing alkyl chains of variable length and found that those with alkoxy groups adopt a liquid crystalline state at varying temperatures depending on the alkyl chain length.[29,30] In contrast, OC12-salpn, a salen derivative with a methyl group introduced as steric bulk, exhibited cold crystallization.[31] Cold crystallization is a phenomenon whereby a molecule that has been cooled to a supercooled liquid or glassy state crystallizes exothermically upon heating. Because the process involves supercooling, cold crystallization materials are expected to be applied as latent heat storage materials. Polyethylene terephthalate (PET) is an example of a cold crystallization material.[32–34] Polymers are generally prone to cold crystallization as their long molecular chains and purity variation impede the assembly of uniform structures. As a result, polymers often adopt an amorphous state, which undergoes glass transition upon heating, followed by exothermic cold crystallization.

While the cold crystallization of polymers is well documented,[35–37] reports on the cold crystallization of small molecules are scarce.[38–41] The existing literature suggests that the rotation of aromatic groups hinders crystallization upon cooling, and that molecular flexibility is an important factor for cold crystallization. Nonetheless, the cold crystallization of Schiff-base nickel complexes without aromatic groups, such as OC12-salpn, has been reported.[31,42,43] In the study of OC12-salpn, the steric hindrance of the methyl group on the chiral carbon was thought to play a major role in slowing down the crystallization rate and causing cold crystallization. In this study, we investigated the thermal behavior of OC*n*-salmpn (Fig. 1), in which the carbon of the ethylenediamine moiety is quaternary, bearing two methyl groups. OC*n*-salmpn complexes do not contain rotatable aromatic groups, but some undergo cold crystallization depending on the alkyl chain length. In this study, the two methyl groups hindered crystallization, leading to cold crystallization. In addition to cold crystallization, the thermal behavior of these complexes included a normal phase transition and oiliness. It is

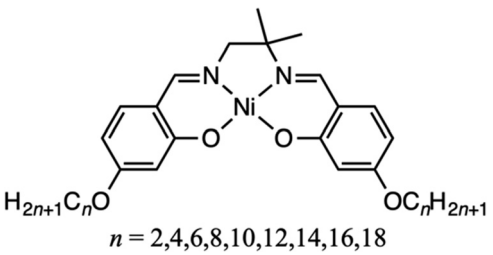

Fig. 1 General chemical structure of OC*n*-salmpn complexes.

Department of Chemistry, Faculty of Science, Tokyo University of Science, 1-3 Kagurazaka, Shinjuku, Tokyo 162-8601, Japan. E-mail: 1319701@ed.tus.acjp, miyamura@rs.kagu.tus.ac.jp

† Electronic supplementary information (ESI) available: Powder XRD, DSC diagrams, optical microscopic images. See DOI: https://doi.org/10.1039/d2ce00305h

suggested that the thermal behavior and assembled structure are controlled by the length of the alkoxy chain. Controlling heat dissipation is an important factor for the development of new materials. Controlling heat dissipation in heat utilization is crucial for the practical application of latent heat storage materials. Therefore, the purpose of this study was to control the thermal behavior and investigate the influence of the alkyl chain length on material design.

Experimental

Materials

All reagents were purchased from Tokyo Chemical Industry (TCI) or Sigma-Aldrich and were used without further purification. ^{1}H NMR spectra were recorded on a JEOL JNM-AL300 spectrometer at 25 °C. Elemental analyses were performed using a Perkin Elmer 2400II CHN analyzer. X-ray diffraction patterns were measured using a Rigaku RINT 2000 instrument.

Synthesis of OC2-salmpn

Nickel(II) acetate tetrahydrate ($Ni(CH_3COO)_2{\cdot}4H_2O$, 2.49 g, 10 mmol) and 1,2-diamino-2-metylpropane (0.88 g, 10 mmol) were added to 100 mL of methanol. The solution was then stirred for 30 min at room temperature, followed by the addition of 2,4-dihydroxybenzaldehyde (2.76 g, 20 mmol). The mixture was refluxed for 4 h and then cooled to room temperature. The red precipitate that formed was collected by suction filtration, providing 3.42 g (yield: 89%) of crude [[*N*, *N*′-bis-(4-alkoxysalicylidene)]-1,2-diamino-2-metylpropanato] nickel(II) (OH-salmpn) as a red powder. This red powder (0.96 g, 3 mmol) and potassium carbonate (K_2CO_3, 1.00 g, 7 mmol) were added to 40 mL of *N*,*N*′-dimethylformamide. The suspension was then stirred for 30 min at room temperature. Then, 1-bromoethane (0.65 g, 6 mmol) was added to the suspension. The suspension was stirred at 80 °C, for 10 h then cooled to room temperature. The mixture was extracted using chloroform and water. The chloroform extracts were dried over $MgSO_4$, filtered and the solvent removed under reduced pressure. The resultant residue was purified using silica gel column chromatography. After evaporation, OC2-salmpn was obtained as red crystals. Yield: 0.06 g (4%); ^{1}HNMR ($CDCl_3$, 400 MHz): σ 7.26 (s, 2H, N═CH), 6.97 (t, J = 8.5 Hz, $2H_{arom}$), 6.50 (t, J = 2.5 Hz, $2H_{arom}$), 6.18 (t, J = 2.6 Hz, $1H_{arom}$), 6.16 (t, J = 2.6 Hz, $1H_{arom}$) 3.97 (q, J = 7.0 Hz, 4H, O–CH_2), 3.15 (s, 2H, C═N–CH_2), 1.45 (s, 1H, N–C–CH_3), 1.37 (t, J = 7.0 Hz, 6H, –CH_3); IR (KBr): ν 1607 cm^{-1} (C═N), 2930 (C–H), 3024 (C–H_{arom}); elemental analysis for $C_{22}H_{26}N_2NiO_4$, calc: C, 59.90; H, 5.94; N, 6.35%, found: C, 58.96; H, 5.64; N, 6.06%.

Synthesis of OC4-salmpn·$CHCl_3$, OC6-salmpn·$CHCl_3$, OC8-salmpn, OC10-salmpn, OC12-salmpn, OC14-salmpn, OC16-salmpn, OC18-salmpn

All title alkyl-substituted [[*N*,*N*′-bis-(2′,4′-dihydroxybenzylidene)]-1,2-diamino-2-metylpropanato] nickel(II) complexes were prepared employing the same procedure as described above for OC2-salmpn using appropriate 1-bromoalkanes instead of 1-bromoethane. OC4-salmpn·$CHCl_3$: yield: 0.42 g (21%); elemental analysis for $C_{27}H_{35}Cl_3N_2NiO_4$, calc: C, 52.59; H, 5.72; N, 4.54%, found: C, 52.39; H, 5.48; N, 4.51%. OC6-salmpn·$CHCl_3$: yield: 0.34 g (16%); elemental analysis for $C_{31}H_{43}Cl_3N_2NiO_4$, calc: C, 55.35; H, 6.44; N, 4.16%, found: C, 55.15; H, 6.77; N, 4.12%. OC8-salmpn: yield: 0.35 g (17%); elemental analysis for $C_{34}H_{50}NiO_4$, calc: C, 67.00; H, 8.27; N, 4.60%, found: C, 67.05; H, 8.32; N, 4.63%; ^{1}HNMR ($CDCl_3$, 400 MHz): σ 7.26 (s, 2H, N═CH), 6.96 (t, J = 8.5 Hz, $2H_{arom}$), 6.50 (t, J = 2.6 Hz, $2H_{arom}$), 6.18 (t, J = 2.6 Hz, $1H_{arom}$), 6.16 (t, J = 2.6 Hz, $1H_{arom}$) 3.90 (t, J = 6.6 Hz, 4H, O–CH_2), 3.15 (s, 2H, C═N–CH_2), 1.74 (quin, J = 7.0 Hz, O–C–CH_2), 1.45–1.28 (m, 26H, C–CH_2–C, N–C–CH_3) 0.89 (t, J = 6.9 Hz, 6H, –CH_3); IR (KBr): ν 1607 cm^{-1} (C═N), 2919 (C–H), 3020 (C–H_{arom}). OC10-salmpn: yield: 0.39 g (17%); elemental analysis for $C_{38}H_{58}NiO_4$, calc: C, 68.57; H, 8.78; N, 4.21%, found: C, 68.34; H, 8.89; N, 4.31%; ^{1}HNMR ($CDCl_3$, 400 MHz): σ 7.26 (s, 2H, N═CH), 6.96 (t, J = 8.6 Hz, $2H_{arom}$), 6.50 (t, J = 2.6 Hz, $2H_{arom}$), 6.18 (t, J = 2.6 Hz, $1H_{arom}$), 6.16 (t, J = 2.6 Hz, $1H_{arom}$) 3.89 (t, J = 6.6 Hz, 4H, O–CH_2), 3.15 (s, 2H, C═N–CH_2), 1.74 (quin, J = 7.0 Hz, O–C–CH_2), 1.45–1.27 (m, 34H, C–CH_2–C, N–C–CH_3) 0.88 (t, J = 6.9 Hz, 6H, –CH_3); IR (KBr): ν 1603 cm^{-1} (C═N), 2920 (C–H), 3021 (C–H_{arom}). OC12-salmpn: yield: 0.29 g (12%); elemental analysis for $C_{42}H_{64}NiO_4$, calc: C, 69.90; H, 9.22; N, 3.88%, found: C, 69.59; H, 9.21; N, 3.70%; ^{1}HNMR ($CDCl_3$, 400 MHz): σ 7.26 (s, 2H, N═CH), 6.96 (t, J = 8. 6 Hz, $2H_{arom}$), 6.50 (t, J = 2.6 Hz, $2H_{arom}$), 6.19 (t, J = 2.6 Hz, $1H_{arom}$), 6.16 (t, J = 2.6 Hz, $1H_{arom}$) 3.89 (t, J = 6.6 Hz, 4H, O–CH_2), 3.15 (s, 2H, C═N–CH_2), 1.74 (quin, J = 7.0 Hz, O–C–CH_2), 1.45–1.26 (m, 42H, C–CH_2–C, N–C–CH_3) 0.88 (t, J = 6.8 Hz, 6H, –CH_3); IR (KBr): ν 1603 cm^{-1} (C═N), 2923 (C–H), 3020 (C–H_{arom}). OC14-salmpn: yield: 0.34 g (15%); elemental analysis for $C_{46}H_{72}NiO_4$, calc: C, 71.03; H, 9.59; N, 3.60%, found: C, 71.07; H, 9.75; N, 3.72%; ^{1}HNMR ($CDCl_3$, 400 MHz): σ 7.26 (s, 2H, N═CH), 6.96 (t, J = 8.6 Hz, $2H_{arom}$), 6.50 (t, J = 2.7 Hz, $2H_{arom}$), 6.19 (t, J = 2.6 Hz, $1H_{arom}$), 6.16 (t, J = 2.6 Hz, $1H_{arom}$) 3.89 (t, J = 6.6 Hz, 4H, O–CH_2), 3.15 (s, 2H, C═N–CH_2), 1.74 (quin, J = 7.0 Hz, O–C–CH_2), 1.45–1.26 (m, 50H, C–CH_2–C, N–C–CH_3) 0.88 (t, J = 6.8 Hz, 6H, –CH_3); IR (KBr): ν 1603 cm^{-1} (C═N), 2916 (C–H), 3021 (C–H_{arom}). OC16-salmpn: yield: 0.31 g (14%); elemental analysis for $C_{50}H_{80}NiO_4$, calc: C, 72.02; H, 9.91; N, 3.36%, found: C, 72.04; H, 9.97; N, 3.33%; ^{1}HNMR ($CDCl_3$, 400 MHz): σ 7.26 (s, 2H, N═CH), 6.96 (t, J = 8.5 Hz, $2H_{arom}$), 6.50 (t, J = 2.6 Hz, $2H_{arom}$), 6.18 (t, J = 2.5 Hz, $1H_{arom}$), 6.16 (t, J = 2.5 Hz, $1H_{arom}$) 3.89 (t, J = 6.6 Hz, 4H, O–CH_2), 3.15 (s, 2H, C═N–CH_2), 1.74 (quin, J = 7.0 Hz, O–C–CH_2), 1.45–1.26 (m, 58H, C–CH_2–C, N–C–CH_3) 0.88 (t, J = 6.8 Hz, 6H, –CH_3); IR (KBr): ν 1603 cm^{-1} (C═N), 2920 (C–H), 3025 (C–H_{arom}). OC18-salmpn: yield: 0.34 g (17%); elemental analysis for $C_{54}H_{88}NiO_4$, calc: C, 72.87; H, 10.19; N, 3.15%, found: C, 72.84; H, 10.50; N, 3.06%; ^{1}HNMR ($CDCl_3$, 400

MHz): σ 7.26 (s, 2H, N═CH), 6.96 (t, J = 8.5 Hz, 2H$_{arom}$), 6.50 (t, J = 2.6 Hz, 2H$_{arom}$), 6.18 (t, J = 2.5 Hz, 1H$_{arom}$), 6.16 (t, J = 2.5 Hz, 1H$_{arom}$) 3.89 (t, J = 6.6 Hz, 4H, O–CH$_2$), 3.15 (s, 2H, C═N–CH$_2$), 1.74 (quin, J = 7.0 Hz, O–C–CH$_2$), 1.45–1.26 (m, 66H, C–CH$_2$–C, N–C–CH$_3$) 0.88 (t, J = 6.8 Hz, 6H, –CH$_3$); IR (KBr): ν 1604 cm^{-1} (C═N), 2919 (C–H), 3024 (C–H$_{arom}$).

Synthesis of OC4-salmpn, OC6-salmpn

After synthesis of OC4-salmpn·CHCl$_3$ and OC6-salmpn·CHCl$_3$ *via* the above-described method, OC4-salmpn and OC6-salmpn were obtained by recrystallization from acetone. OC4-salmpn: yield: 0.37 g (22%); elemental analysis for $C_{26}H_{34}NiO_4$, calc: C, 62.80; H, 6.89; N, 5.63%, found: C, 62.59; H, 6.58; N, 5.51%; ^{1}HNMR ($CDCl_3$, 400 MHz): σ 7.26 (s, 2H, N═CH), 6.96 (t, J = 8.7 Hz, 2H$_{arom}$), 6.50 (t, J = 2.3 Hz, 2H$_{arom}$), 6.18 (t, J = 3.0 Hz, 1H$_{arom}$), 6.16 (t, J = 3.0 Hz, 1H$_{arom}$) 3.91 (t, J = 6.6 Hz, 4H, O–CH$_2$), 3.15 (s, 2H, C═N–CH$_2$), 1.73 (quin, J = 7.0 Hz, O–C–CH$_2$), 1.50–1.40 (m, 10H, C–CH$_2$–C, N–C–CH$_3$) 0.95 (t, J = 7.4 Hz, 6H, –CH$_3$); IR (KBr): ν 1603 cm^{-1} (C═N), 2915 (C–H), 3024 (C–H$_{arom}$). OC6-salmpn: yield: 0.36 g (21%); elemental analysis for $C_{30}H_{42}NiO_4$, calc: C, 59.90; H, 5.94; N, 6.35%, found: C, 64.82; H, 7.39; N, 4.95%; ^{1}HNMR ($CDCl_3$, 400 MHz): σ 7.26 (s, 2H, N═CH), 6.96 (t, J = 8.6 Hz, 2H$_{arom}$), 6.50 (t, J = 2.3 Hz, 2H$_{arom}$), 6.18 (t, J = 2.7 Hz, 1H$_{arom}$), 6.16 (t, J = 2.7 Hz, 1H$_{arom}$) 3.90 (t, J = 6.6 Hz, 4H, O–CH$_2$), 3.15 (s, 2H, C═N–CH$_2$), 1.73 (quin, J = 7.0 Hz, O–C–CH$_2$), 1.45–1.26 (m, 18H, C–CH$_2$–C, N–C–CH$_3$) 0.90 (t, J = 6.9 Hz, 6H, –CH$_3$); IR (KBr): ν 1610 cm^{-1} (C═N), 2930 (C–H), 3020 (C–H$_{arom}$).

Analyses of thermal behavior

Differential scanning calorimetry (DSC) was performed using a NETZSCH DSC 3500 Sirius instrument. The powder crystals of OC*n*-salmpn were enclosed in aluminum sample pans, and DSC scans were performed under dry nitrogen gas. The heating and cooling rates were 5 °C min^{-1}. Optical microscopic data were recorded using a Nikon ECLIPSE LV100POL and a heat stage (Linkam, THMS600). OC*n*-salmpn was inserted between cover glass, and the temperature was controlled by the heat stage in the same manner as for the DSC scans. Microscopic images of the thermal behavior were then collected.

Results and discussion

The thermal behavior of OC*n*-salmpn complexes (n = 2, 4, 6, 8, 10, 12, 14, 16, 18) was evaluated employing differential scanning calorimetry (DSC) and the results are shown in Fig. 2. After melting, the n = 2, 4 samples underwent glass transition only (no crystallization); those with n = 6, 8, 10 exhibited cold crystallization; and the n = 12, 14, 16, 18 complexes displayed typical thermal behavior (crystallization upon cooling).

The DSC curves for the 1st heating/cooling and 2nd heating processes of OC6-salmpn from the "Intermediate" group indicating the exothermic/endothermic peaks are shown in Fig. 3. In the first heating process, OC6-salmpn was heated at a rate of 5 °C min^{-1} and melted at 150.9 °C (peak *a*), displaying an endothermic peak value of 24 kJ mol^{-1} upon changing to a liquid state. When OC6-salmpn was cooled at a rate of 5 °C min^{-1}, it became a supercooled liquid without producing an exothermic peak, which suggests crystallization. Upon further cooling, a baseline shift due to a glass transition occurred at 43.1 °C, and the liquid state became glassy. In the second heating process, a glass transition was observed at 37.2 °C, and the sample changed to a liquid state. Upon further heating, a 17.0 kJ mol^{-1} exothermic peak of appeared at 102.1 °C (peak *b*), and cold crystallization was observed. Cold crystallization refers to heat generation during the heating process. Following cold crystallization, a melting peak corresponding to 22.7 kJ mol^{-1} appeared at 151.4 °C (peak *c*). Since polymorphs probably exist in OC6-salmpn, each of them melts and two endothermic peaks are observed. Detailed powder X-ray analysis around 140–155 °C showed no evidence of stepwise melting (Fig. S1†).

When cooling and heating were repeated thereafter, the thermal behavior was reproducible and identical to that of the first cooling and second heating processes. The DSC curves for OC8-salmpn and OC10-salmpn are shown in Fig. S2 and S3.† No peaks were observed during the cooling of OC8-salmpn, and a glass transition was observed at 29.9 °C. In the second heating process, a glass transition was observed at 30.5 °C and a liquid state was formed. Upon further heating, a 14.4 kJ mol^{-1} exothermic peak appeared at

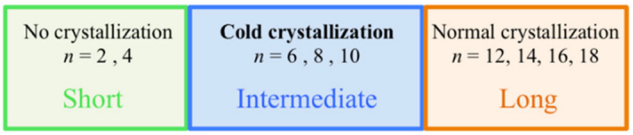

Fig. 2 Variable thermal behavior of OC*n*-salmpn complexes.

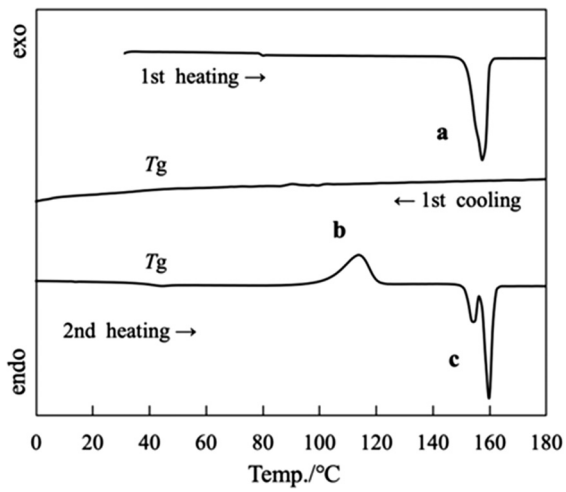

Fig. 3 DSC curves for OC6-salmpn; heating and cooling rate: 5 °C min^{-1}.

72.5 °C, and cold crystallization was observed. A melting peak with a value of 21.2 kJ mol^{-1} appeared at 134.0 °C. No peaks appeared during the cooling of OC10-salmpn, and a glass transition was observed at 19.1 °C. In the second heating process, a glass transition occurred at 15.4 °C, formation of the liquid state was observed, and a 12.8 kJ mol^{-1} exothermic peak appeared at 58.8 °C (cold crystallization). A melting peak with a value of 20.3 kJ mol^{-1} appeared at 132.1 °C.

The most notable difference between the DSC diagrams of OC6-salmpn, OC8-salmpn, and OC10-salmpn was the temperature at which glass transition and cold crystallization occurred, whereas there were no significant differences in the melting point. Although the kinetics of cold crystallization are chain-length-dependent, the thermal stability of the formed crystals did not differ significantly for the range of chain lengths.

To study the cold crystallization behavior in detail, optical images of OC6-salmpn were recorded using an optical microscope equipped with a temperature-controlled stage. During the initial heating process, OC6-salmpn melted at approximately 150 °C and was found to be in an isotropic liquid state (Fig. 4a). Afterwards, the microscopic image remained dark and the isotropic liquid state was retained even after cooling down to 20 °C (Fig. 4b). During the second heating process from 100 to 120 °C, OC6-salmpn crystallized and changed to an anisotropic crystalline state, as shown in Fig. 4c, and finally, it melted into an isotropic liquid state at approximately 150 °C. The onset of cold crystallization was also confirmed in the polarized light microscopy images.

To investigate the phase transition in detail, the structural change during cold crystallization was analyzed employing powder X-ray diffractometry (XRD) with CuKα radiation, and the XRD patterns are shown in Fig. 5 The diffraction pattern of OC6-salmpn at 25 °C after cooling showed a broad peak (halo) at approximately 2θ = 20°, suggesting that it was in an amorphous state. After heating to 130 °C (after peak *b*), the diffraction pattern indicated a crystalline state, confirming that the peaks in the DSC diagram were due to cold crystallization. Polarized light microscopy and powder XRD analysis were also performed to investigate the cold crystallization behavior of OC8-salmpn and OC10-salmpn in detail. During the heating process at 170 °C, the microscopic images (Fig. S4a and S5a†) became darker and the molecules became an isotropic liquid state. During the cooling process at 20 °C, the microscopic images (Fig. S4b and S5b†) were

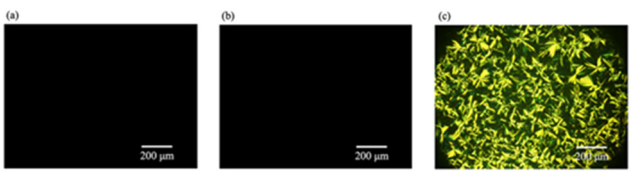

Fig. 4 Optical microscopic images of OC6-salmpn (a) melted isotropic liquid state at 170 °C upon 1st heating, and (b) isotropic supercooled liquid state under T_g, and (c) cold crystallized state at 130 °C during 2nd heating.

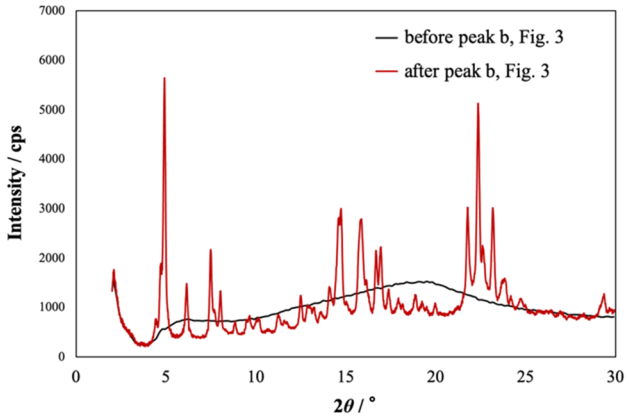

Fig. 5 X-ray diffraction patterns of OC6-salmpn. Black line: at 25 °C during heating (before peak *b*). Red line: upon heating to 130 °C (after peak *b*).

lightly colored and not completely dark, suggesting partial crystallization. To investigate the crystals in detail, powder XRD analysis revealed peaks at 2θ = 4.4° for OC8-salmpn and at 2θ = 3.8°, 7.3°, and 12.7° for OC10-salmpn (Fig. S6 and S7†). The polarized light microscopy images (Fig. S4c and S5c†) and diffraction patterns recorded at approximately 100 °C (after the peak) showed crystal growth. In summary, cold crystallization was observed for OC8-salmpn and OC10-salmpn, whereby the liquid was not completely supercooled but crystallized slightly upon cooling, and the crystals grew exothermically during the heating process. The melting temperature, melting enthalpy, glass transition temperature, cold crystallization temperature, and cold crystallization enthalpy of OC6-salmpn, OC8-salmpn, and OC10-salmpn are listed in Table S1.†

In order to evaluate the stability of this complex in the supercooled metastable phase, OC6-salmpn in glassy state was left at room temperature for one year and DSC measurements were performed (Fig. 6). In the first heating

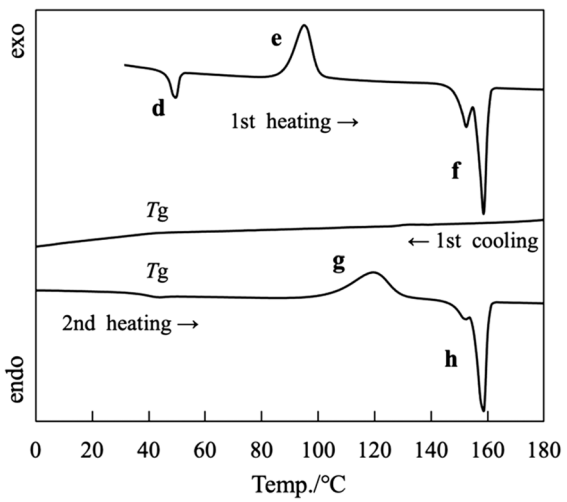

Fig. 6 DSC curves of OC6-salmpn left in glass state for 1 year; heating and cooling rate: 5 °C min^{-1}.

process, an endothermic peak of 2.8 kJ mol^{-1} was observed at 46.5 °C (peak *d*). An exothermic peak of 12.2 kJ mol^{-1} was then observed at 88.0 °C (peak *e*), indicating the cold crystallization. Then, it melted at 155.0 °C (peak *f*) with an endothermic peak of 15.7 kJ mol^{-1}. Only a glass transition was observed during the cooling process, indicating that OC6-salmpn adopted a supercooled state. In the second heating process, the corresponding glass transition was observed. Then, OC6-salmpn compounds cold-crystallized at 103.3 °C (peak *g*) with an exotherm of 13.0 kJ mol^{-1}, and melted at 154.4 °C (peak *h*) with an endotherm of 14.3 kJ mol^{-1}. Compared to normal DSC scans of OC6-salmpn (Fig. 3), OC6-salmpn left in the glassy state for one year underwent a glass transition with enthalpy relaxation (peak *d*), and the cold crystallization temperature shifted to the lower temperature. This cold crystallization suggests that the glassy state of OC6-salmpn is very stable, maintaining a supercooled metastable phase for one year. The good long-term performance and the stability of the supercooled state in cold crystallization behavior are very important to the development of new materials.[44–46] Therefore, the long-term stability of the glassy state in this study suggests that OC6-salmpn is a good heat-storage material.

The DSC curves for OC4-salmpn ("Short" group) obtained during the 1st heating/cooling and 2nd heating processes are shown in Fig. 7. During the first heating process at a rate of 5 °C min^{-1}, OC4-salmpn melted at 94.9 °C and became liquid with an endothermic peak (*i*) value of 42.1 kJ mol^{-1}. Then, when it was cooled at 5 °C min^{-1}, an exothermic peak was not observed, which may be due to crystallization, and it became a supercooled liquid. Upon further cooling, a baseline shift occurred at 49.6 °C arising from the glass transition and a glassy state was attained. During the second heating process, a glass transition was observed at 44.9 °C, and the sample transition to a liquid state. Upon further heating, no exothermic peaks were observed, suggesting no crystallization. Also in the case of OC2-salmpn, only a glass transition was observed in the DSC curve after melting, and crystallization did not occur (Fig. S8†). The melting temperature, melting enthalpy, and glass transition temperature of OC4-salmpn and OC2-salmpn are listed in Table S2.†

The DSC curves for OC14-salmpn ("Long" group) recorded during the 1st heating/cooling and 2nd heating processes are depicted in Fig. 8. During the first heating process at a rate of 5 °C min^{-1}, OC14-salmpn melted and became liquid at 129.6 °C with an endothermic peak (*j*) value of 46.8 kJ mol^{-1}. Then, OC14-salmpn crystallized at 83.6 °C with an exothermic peak value of 42.0 kJ mol^{-1} (peak *k*) when cooled at 5 °C min^{-1}. During the second heating process, it melted at 126.5 °C and at 133.8 °C with endothermic peak (*l* and *m*) values of 41.5 and 0.9 kJ mol^{-1}, respectively. When cooling and heating were repeated thereafter, the thermal behavior was reproducible and identical to that of the first and second cooling processes. Typical thermal behavior, namely melting with heating and crystallization with cooling, was observed for OC12-salmpn (Fig. S9†), OC16-salmpn (Fig. S10†), and OC18-salmpn (Fig. S11†). The phase transition temperatures and enthalpies of the three "Long" samples are listed in Table S3.†

The relationship between the phase transition temperatures of the OC*n*-salmpn complexes (*n* = 2, 4, 6, 8, 10, 12, 14, 16, 18) and the chain length is illustrated in Fig. 9, showing the 1st cooling freezing points (yellow-green), 2nd heating cold crystallization temperatures (blue), melting points (red), and glass transition temperatures (orange). While it did not influence the melting point significantly, the chain length clearly affected the freezing point, cold crystallization temperature, and glass transition temperature. Kinetically, the higher the cold crystallization temperature, the longer crystallization is delayed. In other words, as the alkyl chains become shorter, cohesion between them decreases. This is thought to be due to the weakening of the van der Waals forces among the alkyl chains. Regarding the glass transition point, it is suggested that as the alkyl chains

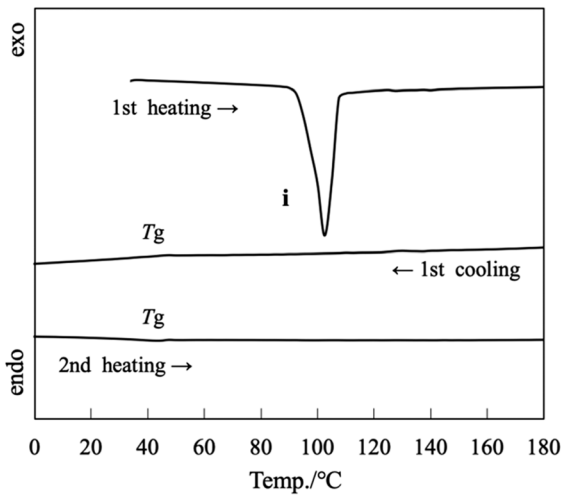

Fig. 7 DSC curves for OC4-salmpn; heating and cooling rate: 5 °C min^{-1}.

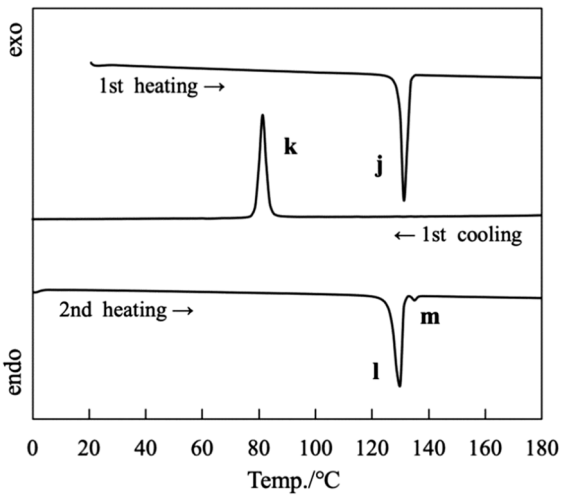

Fig. 8 DSC curves for OC14-salmpn; heating and cooling rate: 5 °C min^{-1}.

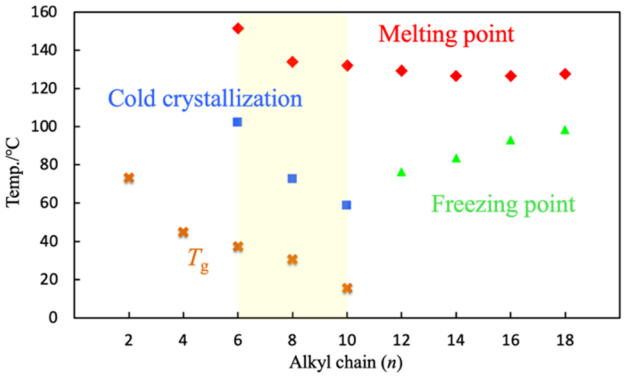

Fig. 9 Dependence of OC*n*-salmpn phase transition temperatures on the alkyl chain length.

become shorter, the temperature at which molecular mobility is prevented increases.

When OC6-salmpn and OC4-salmpn were recrystallized from chloroform/methanol, the elemental analysis results indicated that one complex molecule contained one chloroform molecule; thus, the obtained crystal were designated as OC6-salmpn·$CHCl_3$ and OC4-salmpn·$CHCl_3$. Thermogravimetric analysis (TGA) of OC6-salmpn·$CHCl_3$ and OC4-salmpn·$CHCl_3$ was performed to observe the elimination of chloroform molecules. When the two samples were heated at a rate of 5 °C min^{-1}, their weight decreased as shown in Fig. 10(a) and (b). In the case of OC6-salmpn·$CHCl_3$, chloroform desorption from the crystals commenced at approximately 60 °C and complete elimination occurred at approximately 130 °C. The weight loss due to chloroform elimination was estimated to be 15%, which is consistent with the XRD and elemental analysis results for the amount of chloroform molecules contained in the crystals. Chloroform began desorbing from OC4-salmpn·$CHCl_3$ at approximately 90 °C and was completely eliminated at approximately 165 °C. The weight loss due to chloroform elimination was estimated to be 20%, which is consistent with the XRD and elemental analysis results for the amount of chloroform molecules contained in the crystals.

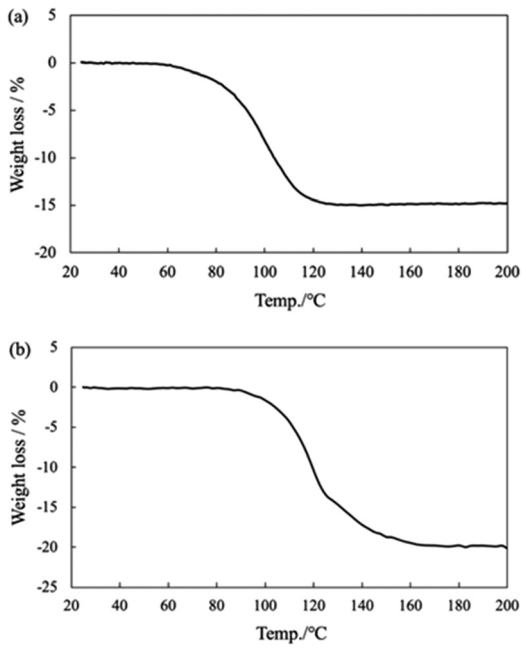

Fig. 10 TG traces of (a) OC6-salmpn·$CHCl_3$ and (b) OC4-salmpn·$CHCl_3$ at a heating rate of 5 °C min^{-1}.

Fig. S12a and S13† shows the DSC curves of OC6-salmpn·$CHCl_3$ and OC4-salmpn·$CHCl_3$ crystals recorded in an open system: DSC curves were measured using aluminum sample pans without lids. When OC6-salmpn·$CHCl_3$ crystals were heated at a rate of 5 °C, phase transition to OC6-salmpn was observed at 80–120 °C, giving rise to a broad endothermic peak due to the exclusion of chloroform molecules. Subsequent to that, the thermal behavior was the same as that of OC6-salmpn, and cold crystallization occurred. Powder X-ray structure analysis of the simulated single crystal structure, OC6-salmpn·$CHCl_3$, and OC6-salmpn desorption and the pattern in Fig. 5 (red curve) were shown in Fig. S12b.†

When the OC4-salmpn·$CHCl_3$ crystal was heated at a rate of 5 °C min^{-1}, a large and broad endothermic peak was observed in the range of 90–150 °C, as shown in Fig. S13.† Such a peak shape likely arises due to the simultaneous endothermic processes of chloroform exclusion and melting. Subsequent to that, it behaves in the same manner as the OC4-salmpn melt, and does not undergo crystallization during the cooling process or the second heating process.

Conclusions

OC*n*-salmpn (n = 2, 4, 6, 8, 10, 12, 14, 16, 18) complexes exhibited complex and dissimilar thermal behavior: for n = 2, 4, only a glass transition was observed and no crystallization occurred after melting; the n = 6, 8, 10 complexes displayed cold crystallization; and normal thermal behavior was noted for n = 12, 14, 16, 18. The two methyls on the quaternary carbons of OC*n*-salmpn are considered to be steric hindrances, most likely causing the supercooled state. In addition, cold crystallization occurred in n = 6, 8, and 10. OC*n*-salmpn complexes with controlled heat dissipation have potential applicability as latent heat storage materials. In addition, because the temperature at which cold crystallization occurs is distinct between n = 6, 8, and 10, it is possible to control the temperature of heat storage as needed. The melting point of all the OC*n*-salmpn complexes is >130 °C, allowing for broader applicability, such as heat storage materials used in automobiles and boiler systems.

Conflicts of interest

There are no conflicts to declare.

Notes and references

1 Y. Han, H. T. Cao, H. Z. Sun, Y. Wu, G. G. Shan, Z. M. Su, X. G. Hou and Y. Liao, *J. Mater. Chem. C*, 2014, **2**, 7648.

2 K. P. Goetz, K. Sekine, F. Paulus, Y. Zhong, D. Roth, D. Becker-Koch, Y. J. Hofstetter, E. Michel, L. Reichert, F. Rominger, M. Rudolph, S. Huettner, Y. Vaynzof, E. M. Herzig, A. S. K. Hashmi and J. Zaumseil, *J. Mater. Chem. C*, 2019, **7**, 13493.
3 C.-C. Chen, T. Hinoue, J.-H. Liu, I. Hisaki, M. Miyata and N. Tohnai, *Bull. Chem. Soc. Jpn.*, 2014, **87**, 76.
4 A. F. F. Cheung, E. Y. H. Hong and V. W. W. Yam, *Chem. – Eur. J.*, 2018, **24**, 1383.
5 S. Arai, K. Morita, J. Tsutsumi, S. Inoue, M. Tanaka and T. Hasegawa, *Adv. Funct. Mater.*, 2020, **30**, 1906406.
6 N. A. Wazzan, I. B. Obot and S. Kaya, *J. Mol. Liq.*, 2016, **221**, 579.
7 J. Cosby, P. Starck, D. Littlewood, O. O. Mykhaylyk and A. J. Ryan, *J. Colloid Interface Sci.*, 2021, **596**, 442.
8 X. Hao, B. Xiong, M. Ni, B. Tang, Y. Ma, H. Peng, X. Zhou, I. I. Smalyukh and X. Xie, *ACS Appl. Mater. Interfaces*, 2020, **12**, 53058.
9 D. M. Arkhipova, V. V. Ermolaev, V. A. Miluykov, F. G. Valeeva, G. A. Gaynanova, L. Ya. Zakharova, M. E. Minyaev and V. P. Ananikov, *Sustainability*, 2021, **13**, 9862.
10 H. Gao, P. Xue, J. Peng, L. Zhai, M. Sun, J. Sun and R. Lu, *New J. Chem.*, 2019, **43**, 77.
11 Y. Ma, Y. Zhang, L. Kong and J. Yang, *Tetrahedron*, 2019, **75**, 674.
12 K. Ohta, H. Hasebe, M. Moriya, T. Fujimoto and I. Yamamoto, *Mol. Cryst. Liq. Cryst.*, 1991, **208**, 43.
13 I. Abdurrokhman, K. Elamin, O. Danyliv, M. Hasani, J. Swenson and A. Martinelli, *J. Phys. Chem. B*, 2019, **123**, 4044.
14 A. Kawasaki, T. Takeda, N. Hoshino, W. Matsuda, S. Seki and T. Akutagawa, *J. Phys. Chem. C*, 2021, **125**, 21595.
15 E. D. Río, T. Vidil, W. Gati, É. Grau, D. Taton and H. Cramail, *ACS Sustainable Chem. Eng.*, 2021, **9**, 12687.
16 K. Ueji, K. Nomoto, S. Ichimura, S. Shinozaki, K. Abe, K. Tomono, Y. Tamaki and K. Miyamura, *Bull. Chem. Soc. Jpn.*, 2017, **90**, 684.
17 K. Dai, K. Nomoto, S. Ueno, K. Tomono and K. Miyamura, *Bull. Chem. Soc. Jpn.*, 2011, **84**, 312.
18 G. Saito, Y. Yoshida, H. Murofushi, N. Iwasawa, T. Hiramatsu, A. Otsuka, H. Yamochi, K. Isa, E. Mineo-Ota, M. Konno, T. Mori, K. Imaeda and H. Inokuchi, *Bull. Chem. Soc. Jpn.*, 2010, **83**, 335.
19 W. A. Souza, A. M. de Almeida, M. Pivatto, M. V. de Almeida, G. P. Guedes, J. A. L. C. Resende and W. Guerra, *J. Mol. Struct.*, 2021, **1226**, 129250.
20 Q. Wu, X. Jia and M. Wong, *Mater. Today Chem.*, 2022, **23**, 100636.
21 S. J. Prathapa, C. Slabbert, M. A. Fernandes and A. Lemmerer, *CrystEngComm*, 2019, **21**, 41.
22 A. Honda, K. Noda, Y. Tamaki and K. Miyamura, *Materials*, 2016, **9**, 837.
23 D. Bléger, A. Bocheux, D. Kreher, F. Mathevet, A.-J. Attias, G. Metgé, L. Douillard, C. Fiorini-Debuisschert and F. Charra, *Nanoscale*, 2013, **5**, 1452.
24 K. Tahara, R. Nakayama, M. Maeda, S. De Feyter and Y. Tobe, *J. Phys. Chem. C*, 2019, **123**, 27020.
25 M. Maeda, R. Nakayama, S. De Feyter, Y. Tobe and K. Tahara, *Chem. Sci.*, 2020, **11**, 9254.
26 C. Fu, J. Mikšátko, L. Assies, V. Vrkoslav, S. Orlandi, M. Kalbáč, P. Kovaříček, X. Zeng, B. Zhou, L. Muccioli, D. F. Perepichka and E. Orgiu, *ACS Nano*, 2020, **14**, 2956.
27 Y. Tobe, K. Tahara and S. De Feyter, *Chem. Commun.*, 2021, **57**, 962.
28 T. Hu, Y. Wang, M. Dong, J. Wu, X. Miao, Y. Hu and W. Deng, *J. Phys. Chem. C*, 2020, **124**, 1646.
29 I. Aiello, M. Ghedini, F. Neve and D. Pucci, *Chem. Mater.*, 1997, **9**, 2107.
30 Y. Abe, H. Akao, Y. Yoshida, H. Takashima, T. Tanase, H. Mukai and K. Ohta, *Inorg. Chim. Acta*, 2006, **359**, 3147.
31 A. Honda, T. Yoshida, A. Shioda, K. Nomoto and K. Miyamura, *Bull. Chem. Soc. Jpn.*, 2019, **92**, 1853.
32 T. Liu, Z. Mo, S. Wang and H. Zhang, *Polym. Eng. Sci.*, 1997, **37**, 568.
33 Z. Pingping and M. Dezhu, *Eur. Polym. J.*, 1997, **33**, 1817.
34 R. M. R. Wellen and M. S. Rabello, *J. Mater. Sci.*, 2005, **40**, 6099.
35 I. D. dos Santos Silva, H. Schäfer, N. G. Jaques, D. D. Siqueira, A. Ries, D. D. de Souza Morais, K. Haag, K. Koschek, L. H. Carvalho and R. M. R. Wellen, *J. Therm. Anal. Calorim.*, 2020, **141**, 1389.
36 C. H. Xu, J. P. Wang and W. B. Hu, *Chin. J. Polym. Sci.*, 2019, **37**, 627.
37 B. Na, N. N. Tian, R. H. Lv, Z. J. Li, W. F. Xu and Q. Fu, *Polymer*, 2010, **51**, 563.
38 S. Sampath, A. A. Boopathi and A. B. Mandal, *Phys. Chem. Chem. Phys.*, 2016, **18**, 21251.
39 A. Honda, S. Kakihara, M. Kawai, T. Takahashi and K. Miyamura, *Cryst. Growth Des.*, 2021, **21**, 6223.
40 K. Iwase, H. Houjou, Y. Yamamura and K. Saito, *Chem. Lett.*, 2013, **42**, 1040.
41 K. Iwase, Y. Nagano, I. Yoshikawa, H. Houjou, Y. Yamamura and K. Saito, *J. Phys. Chem. C*, 2014, **118**, 27664.
42 Q. Wang, A. Takeuchi, Y. Yamamura, K. Saito, W. Mori and M. Sorai, *J. Phys. Chem. B*, 2008, **112**, 11039.
43 K. Iwase, I. Yoshikawa, H. Houjou, Y. Yamamura and K. Saito, *Bull. Chem. Soc. Jpn.*, 2015, **88**, 989.
44 S. Puupponen and A. Seppälä, *Sol. Energy Mater. Sol. Cells*, 2018, **180**, 59.
45 K. Turunen, M. R. Yazdani, A. Santasalo-Aarnio and A. Seppälä, *Sol. Energy Mater. Sol. Cells*, 2021, **230**, 111273.
46 M. R. Yazdani, J. Etula, J. B. Zimmerman and A. Seppälä, *Green Chem.*, 2020, **22**, 5447.

